Optimization and Analysis of Ultrasonic Wedge Bonding Parameters for Enhanced Bonding Performance in 21700 Cylindrical Lithium Battery Modules

Bin Luo, Mohamad Hanif Md Saad, Altaf Hossain Molla and Zambri Harun*

Department of Mechanical and Manufacturing Engineering, Faculty of Engineering and Built Environment, Universiti Kebangsaan Malaysia, 43600 Bangi, Selangor, Malaysia

ABSTRACT

The 21700 cylindrical lithium battery module uses ultrasonic wedge bonding technology to connect the positive terminal and negative terminal of the cell to the busbars. The weak bond of the negative terminal. This paper studied the wire bonding parameter of the negative terminal (Al wire and Fe-base Ni-top can). We aim to analyze the reasons for the poor bonding performance of the central area of the joint. Through stress and strain simulation, the result shows that the stress at the center region is lower than that in the circumference region, and the high-stress region corresponds to the ridges' vein-shaped elliptical rings of the bonding interface (i.e., the effective bonding area). The model was further validated through experimental design. The unbonded area in the center region of the joint can be limitedly reduced by optimizing key parameters, and the influencing parameters in the order of most to least critical are bond power, force, and time. Shear strength and tensile tests were used to evaluate bonding qualities. The regression equations of Al wire deformation and joint width corresponding to key parameters were established. The optimal range of Al wires deformation and joint width is proposed. The minimum value of the deformation was 174 μm, and the maximum value was 248 μm. The minimum value of the joint width was 560 μm, and the maximum value was 1110 μm. The optimal bonding parameters obtained by the response optimizer are bond force 1250 gf and bond power 100.

INTRODUCTION

Wire bonding technology has been continuously developing since the 1960s. Many scholars have researched ultrasonic welding, and it is still a guided document

for ultrasonic bonding. Their theories are briefly summarized as follows: Harman and Albers (1977) studied Al-Al wedge bonding. The results showed that the bonding started at the periphery of the joint, and as the bond time increased, the effective bonding area gradually expanded toward the center and continued to increase until the entire interface. Sometimes, the center was not bonded, which was related to the wedge-shaped shape. Winchell and Berg (1978) studied the effect of bonding parameters on the bonding point formation process. It is concluded that as the ultrasonic power increases, the effective connection area increases; as the bonding time increases, the effective connection part expands to the central unbonded area; the bond point imprint area increases as the bonding force increases. Zhou et al. (2005) studied Au-Au ultrasonic wedge bonding. It was found that the metallurgical bonding started at both ends of the impression, and the center of the impression also achieved a metallurgical connection. The interface underwent shear deformation, micro-slip, and relative sliding. Since increasing pressure will reduce the connection area of the periphery and center, there is no necessary relationship between joint quality and deformation. Chen et al. (2006) conducted experiments on Al-Ni wedge bonding. The research reveals that the Al-Ni interface formed by ultrasonic bonding was the central unbonded and elliptical interface; refer to Figure 1 for the definitions of the central unbonded and elliptical interface. Previous works (Lum et al., 2005; 2006; Mindlin, 1949) studied the 25 μm diameter gold wire with copper substrate wedge bonding. The micro-slip theory concluded that when the ultrasonic power is small, there is only a micro-slip at the periphery of the bonding interface; when the ultrasonic power is enormous, a macro-slip will occur, and the entire interface will form a bond.

Li et al. (2006) studied the Al-1%Si wire bonded onto the Au/Ni/Cu pad. It was found that the wire was softened by ultrasonic vibration; at the same time, pressure was loaded on the wire, and plastic flow was generated in the bonding wire, which promoted the diffusion of Ni into Al. Ultrasonic vibration enhanced the interdiffusion resulting from inner defects
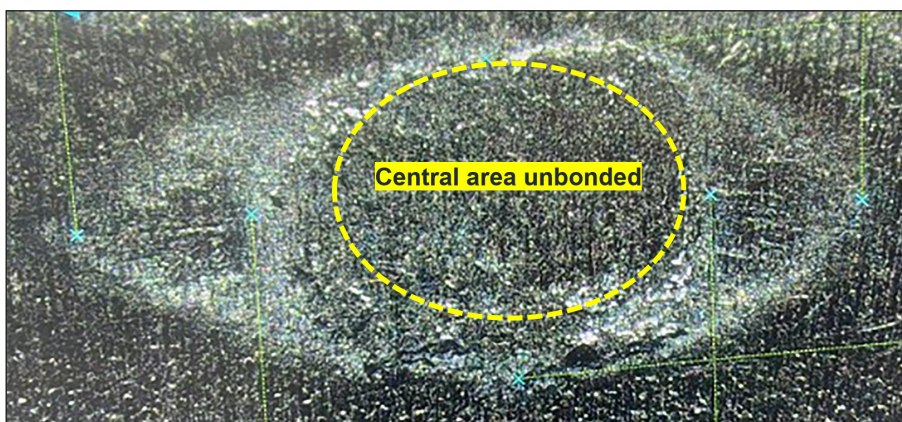

Figure 1. Morphology of the central unbonded area

such as dislocations, vacancies, and voids ascribed to short-circuit diffusion. Li et al. (2007a; 2007b; 2007c) conducted a thermosonic flip chip bonding test between Au bumps and Al and Ag metallization layers, and the results showed that the bonded joint contains several dislocation lines. They believe that a short-circuit diffusion along dislocation lines is the leading cause of interfacial bonding. Therefore, the dynamic effect of ultrasonic vibration is a microscopic joining mechanism that activates many dislocations in the metal lattice. Ji et al. (2005) studied Al-Ni-Cu bonding. It was found that there is an evident diffusion of Ni into Al wire after high-temperature storage at 170°C for 10 days. At age 30 days, the bond interface forms a cloud-like structure, and the primary composition is Al and Ni. At age 40 days, the cloud-like structure transforms into a rectangular island-like structure, and there are many cavities inside the bond wire, which are different from the Kirkendall voids because of the shape and dimension. Ji et al. (2006) It was found that lateral and longitudinal joint marks were observed. The former was perpendicular to the direction of the ultrasonic vibration and distributed at the periphery of the bond interface. However, the latter was parallel to the vibration directions located at the bond center. The features above had an essential influence on bond resistance. The mechanism was ascribed to stress evolution and distribution during the bonding process.

Bieliszczuk et al. (2024a) studied the impact of surface laser cleaning on the properties of the wire-bonded joint in a cylindrical lithium-ion battery pack. The results have shown that laser cleaning with 40% power of the 30 W ATMS4060 laser marker helps to reduce the standard deviation of the shear test results from 16.1% for the uncleaned sample down to 2.6%. Cleaning with 80% of the laser power did not further impact shear test results and almost eliminated oxides from the bonded materials interface. Hamada and Iwamoto (2023) observed the morphology and microstructure of the bond tool with Al adhesion and surface wear. It was found that Al adhered to the area where the vertical load on the bond tool was high during welding. Aluminum oxide and aluminum were present in layers in the adhered wire, indicating that the adhered wires grew due to repeated wire adhesion and destruction processes. Tool wear was related to fretting wear and plastic flow associated with wire deformation.

Researchers also have carried out a lot of research work on the following aspects: measuring the temperature change of the interface during the bonding process (Ho et al., 2004), measuring the vibration amplitude of the bonding tool, measuring the change of the ultrasonic loop signal (Qi et al., 2006), problems with the formation of Kirkendall holes accompanying the growth of intermetallic compound (Chang et al., 2004; Uno & Tatsumi, 2000). The results show that the evolution characteristics of the joint and the interface bonding characteristics are very complex, causing the results to be very divergent, and the microscopic effects of pressure and ultrasound on the bonding material cannot be distinguished. With the support of finite element simulations, fatigue behavior related to the material properties in the bonding wires was investigated (Czerny et al., 2013; Czerny

& Khatibi, 2016). Fatigue lifetime was found to be influenced by wire diameter, junction temperature swing, monitoring current, and aspect ratio of the wedge. The contact and displacement behavior between the wire and the substrate (Schemmel et al., 2018a; Unger et al., 2016;). friction (Long et al., 2020; Schemmel et al., 2018b;), dynamic behavior (Long et al., 2019), and deformation (Li et al., 2019; Tang et al., 2022). However, wire bonding is widely used in the battery industry (Bieliszczuk et al., 2024b; Zwicker et al., 2020). Studies on wedge bonding interface mechanisms and joint quality evaluation of cylindrical batteries are not widely available.

Wire Bonding Process Description

Automotive battery packs for electromobility consist of many interconnected battery cells. The research object of this paper is the 21700 cylindrical lithium battery modules. Here, 21 represents the diameter of the battery, and 70 represents the height of the battery. The cylindrical lithium battery steel shell is called a can (Fe-base Ni-top can), and the connection between the can and the busbar is called the anode bonding (negative terminal). The bonding wire uses aluminum material with a 0.5 mm diameter. The ultrasonic bonder used in this research is the K&S model, ultrasonic frequency 80 kHz. The wedge bonders are driven by constant voltage mode. Bonder "power" parameters correspond to a generator's drive voltage. For large wires, at a max power of 255 (0–255, where 0 counts as 1), the drive voltage is 300 Vpp. The setting unit is level (approximately 1 level = 1.17 V when converted to unit). For example, power level = 100 for 0.5 mm diameter wire, the calculated drive voltage = (100/256) × 300 Vpp = 117.18 Vpp.

Ultrasonic wedge bonding technology of Al wire is used to connect the positive terminal and negative terminal of the battery cells to each busbar, respectively, and then each busbar is connected to the flexible printed circuit board (FPCB) to form the required series-parallel relationship. The weak bond of the negative terminal is the primary failure phenomenon (Figure 2). The failure phenomena include the occurrence when the Al wire is separated from the bond interface and a large area unbonded in the central region of the bonding interface. The morphology of the central unbonded area is shown in Figure 1.

MATERIALS AND METHODS

The main approach of this investigation is to conduct interface morphology, perform finite element analysis (FEA), respond surface methodology (RSM) and test
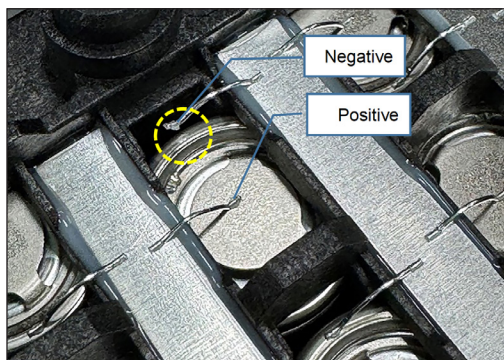

Figure 2. Cylindrical lithium battery module structure negative terminal weak bonded phenomenon

bonding strength on the wedge bonding of the negative terminal (Al wire and Fe-base Ni-plating can shell) in 21700 cylindrical lithium battery modules.

The effect of parameter changes on the central unbonded area of the joint is analyzed using intermetallic layer and vision analysis. The TEM samples were prepared by FIB (focused ion beam), and the bonding characteristics of the ultrasonic wedge-bonded joint interface were observed and analyzed under high-resolution transmission electron microscopy. The ion miller used is the Hitachi ArBlade 5000 model; it achieves ultra-high-speed cross-section grinding. ArBlade 5000 features PLUS II ion gun technology design, and the ion gun emits a high current density ion beam with a cross-section grinding rate of up to 1 mm/h. It uses a wide-area cross-section grinding sample holder with a cross-section grinding width of up to 8 mm. The ion milling system polishes the surface of a sample using the sputtering effect caused by irradiating an argon ion beam on the surface. Unlike mechanical polishing, the ion milling system processes the sample without deforming it or applying mechanical stress. The scanning electron microscope used is Hitachi SU8220, with a cold field electron gun, magnification: 20-1000000X, acceleration voltage: 0.01-30KV, and secondary electron image resolution (0.8nm/15kV). The test sample is based on the 21700-battery assembly process of a company in Nanjing, China, and is commissioned by a Korean institution and equipment for testing.

The finite element analysis (FEA) was used to further analyze the effect of parameter changes on the unbonded area in the center of the joint. The process model was first designed to simulate the deformation of Al wires. Then, the deformation and equivalent plastic strain of the ultrasonic wire bonding process was divided into three physical coupling processes. Firstly, the wire plastically deforms under the force of the tool. Secondly, the tool drives the wire to vibrate at a high frequency in the bonding area. Due to the high-speed friction between the wire and the pad, the oxide layer on the contact surface is fractured. Thirdly, under the effect of ultrasonic power, the wedge part of the wire continuously deforms, and atomic diffusion occurs on the contact interface, forming a stable bonding joint. The ultrasonic bonding process was converted into a numerical calculation process using FEA based on such analysis. The can shell material uses SPCC 0.4 mm thick steel plate as the base material and has a high Young's modulus; hence, a rigid body was used to simulate the mechanical behaviors of bonding. Here, SPCC stands for S-steel, P-plate, C-cold, and C-common. The can shell uses a pre-nickel-plating process. The thickness of the external nickel plating is 3 μm, and the internal nickel plating is 2 μm. The mesh build is essential to the simulation results. Specifically, fine mesh subdivides the areas of Al wires, while the rest of the regions are roughly meshed to accelerate the simulation process. Al wire is defined as a deformable part with an overall meshing size of 0.04 mm, whereas the bond tool and can are modeled as a rigid body with a meshing size of 0.05 mm. For the mesh of the model, a total number of 46167 nodes and 40408 elements. Abaqus software with an explicit solver was applied in this research. The specs of the PC are EX650i 239512-SCC.

The response surface methodology (RSM) was further used in process test verification. The DoE was performed using Minitab software. Shear strength and tensile tests were used to evaluate bonding qualities. A total of 42 normal cell samples with different production dates were randomly selected, and the anode surface was laser-cleaned before testing. There were 10 joints bonded on the anode surface of each cell and 30 joints bonded for each set of parameters, totaling 14 sets of parameters and 420 bonded joints. A digital display tensile tester is used to perform the tensile test. The tensile force is applied to a complete bonding loop, and the tensile force is applied to the highest point of the Al wire bonding loop. A shear strength test is performed using a digital thrust tester until the aluminum wire and the contact are completely separated from the bonding interface.

RESULTS AND DISCUSSION

Bonding Interface Morphology Analysis

Several failed samples were selected for microscopic observations to understand the ultrasonic wedge bonding interface joint characteristics. For the unbonded sample, no. 1 has a noticeable difference in the ratio of the joint and no ridges' vein-shaped elliptical rings (Figure 3a). There are obvious ridges' vein-shaped elliptical rings on the bonding interface of the weakly bonded samples no. 2–4, refer to Figures 3b–3d. The silvery white areas are bonded marks. The morphological characteristics of samples show a common
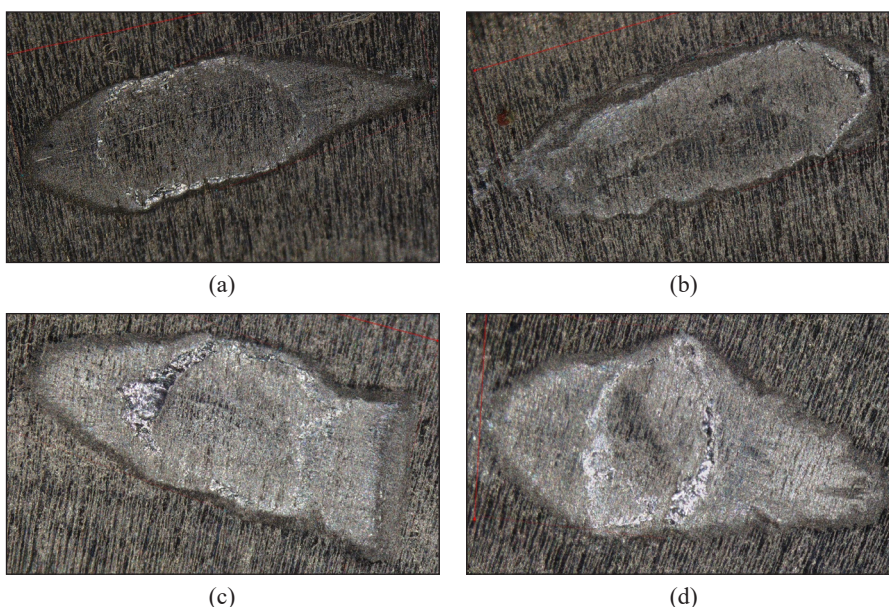

(a)	(b)
(c)	(d)

Figure 3. Morphology of weak bonded samples: (a) No. 1 unbonded; bond force 800 gf, bond time 130 ms, bond power 60; (b) No. 2 strength < 300 gf; bond force 1400 gf, bond time 130 ms, bond power 80; No. 3 strength < 800 gf; bond force 800 gf, bond time 130 ms, bond power 100; (d) No. 4 strength < 1500 gf); bond force 800 gf, bond time 130 ms, bond power 130

feature: the shape of the bonding joint is elliptical. Bonding starts from the periphery of the ellipse and gradually spreads to the central area. The effective bonding area is the ridges' vein-shaped elliptical rings, and the central area is not bonded. The aspect ratio and area of the unbonded area also vary significantly.

Figure 4 shows the cross-sectional morphology of another weakly bonded sample. Figure 4a is the normal bonded joint, and Figure 4b is the weak bonded joint. It shows that the distribution of the diffusion layer of Al atoms in the Ni substrate after bonding is significantly different. The diffusion layer of Al atoms at the weak bonding point is very thin and has a small area. The depth and location of the atomic diffusion layer at the bonding
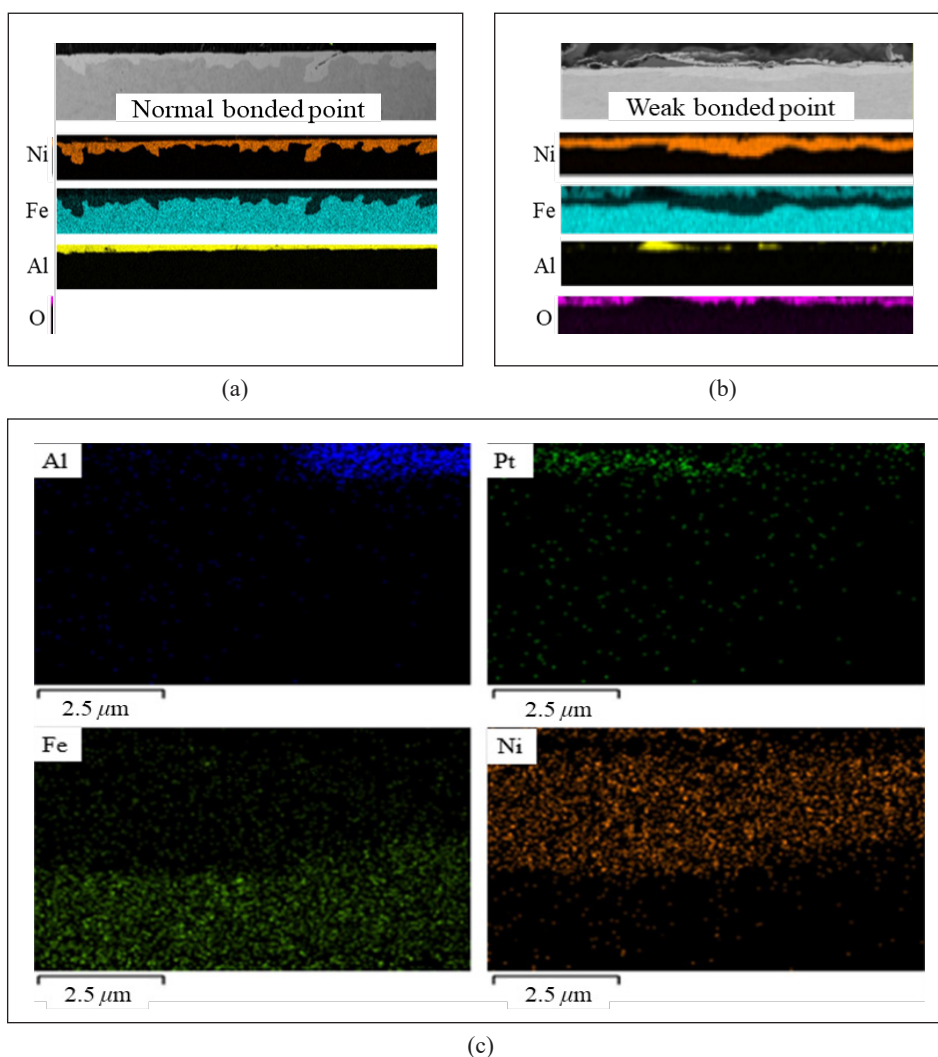

(a)

(b)

(c)

Figure 4. (a) Cross-section of normal bonded joint, (b) cross-section of weak bonded joint, (c) FIB result of weak bonded joint

interface characterize the bonding strength of the joint. The mutual diffusion of Al and Ni atoms produces a solid solution or alloy strengthening in dual material crystals. The bonding interface is a spatial multi-structure (i.e., Al wire-diffusion layer-base material).

At the weak bonding point, in addition to the Al and Ni coatings in a small area at the bonding interface, a large area of Fe and O was detected at the bonding interface. No elements other than Al and Ni were found at the bonding interface at the normal bonded point. Further, a FIB analysis of weakly bonded areas shows the distribution of aluminum, nickel, and iron at the interface in Figure 4c, and no other by-products were observed. However, the presence of the Pt element in the picture may be an element deposited during the FIB sample preparation process. The presence of Fe is suspected to be generated during ion milling.

Through the analysis of the morphological characteristics of the wire bonding interface of cylindrical lithium batteries, the results show that the interface mode of Al-Ni ultrasonic wedge bonding is shaped like a ridged torus, and the center area is unbounded. Ridge wrinkles are high-strength bonding formed by strong physical diffusion under the action of ultrasound. These ridge wrinkles form the bonding strength. So, one can understand the generation of bonding interface strength: the two substances at the bonding interface produce atomic interdiffusion, forming a strong atomic bond. The diffused atoms are solidly dissolved in the Ni matrix, which strengthens the interface microstructure strength, making the bonding interface strength generated by atomic diffusion greater than the strength of the Al wire. Therefore, only Al residues are seen on the separation interface; destruction does not occur in the atomic diffusion layer. It also shows that the interface has a depth range for atomic diffusion. At the same time, the bonding interface inevitably exists as an intermediate phase (compound). The mesophase generated and the impact on bonding quality require further analysis.

Bonding Interface Stress and Plastic Strain Analysis

Bonding parameters are also one of the main reasons for weak bonding. The stress and plastic strain distribution characteristics at the bonding interface in the ultrasonic bonding process and the influence of process parameters on the bonding quality were further analyzed. The major components, such as the bond tool, Al wires and the can, were modeled to focus on wire deformations. A geometric model was established, as shown in Figure 5a. The material of the bond tool was tungsten steel. Figure 5b shows the bond tool's geometry size. Figure 6 shows the stress-strain curve of the component (Al wire) that undergoes large plastic deformation during the simulation. The parameters of Al wire material at room temperature are shown in Table 1.

The ultrasonic vibration system controls the joint quality by adjusting the vibration of the bond tool. The value of ultrasonic power corresponds to sound intensity I. The math between them follows Equation 1.
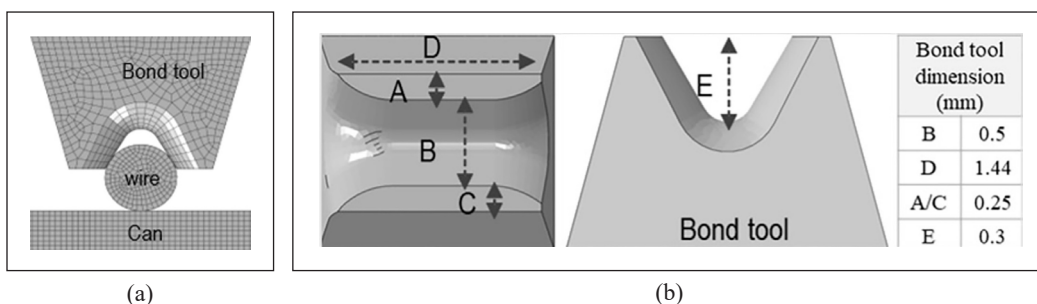
<table>
<tr><td colspan="2">Bond tool
dimension
(mm)</td></tr>
</table>

Bond tool dimension (mm)	
B	0.5
D	1.44
A/C	0.25
E	0.3

(a)   (b)

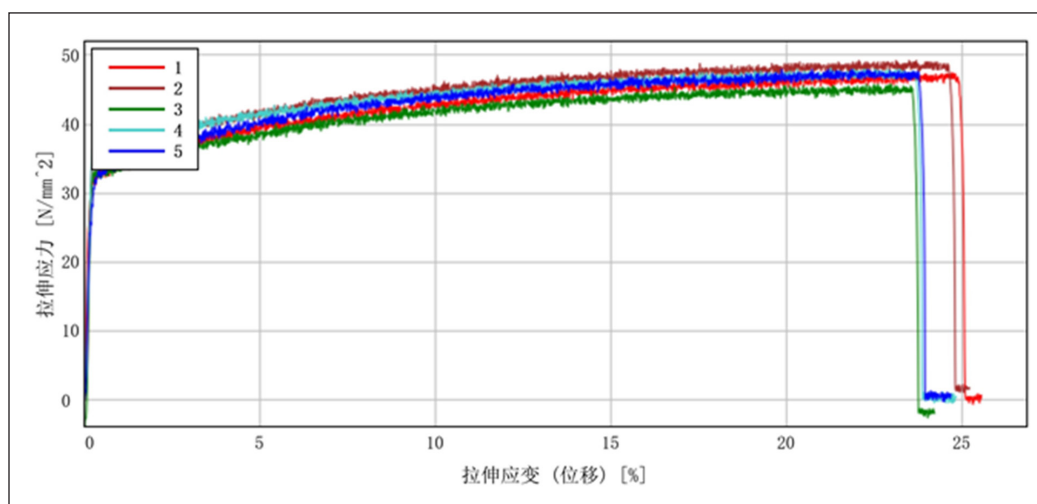*Figure 5*. (a) Geometric model of bonding component; (b) Bond tool shape and key size

Figure 6. Stress-strain curve of Al wire

Table 1
Material parameters in the simulation model

Item	Material	Young's Modulus	Poisson' Ratio	Yield Stress
Al wire	Aluminum (Al 1050) (Diameter 0.5 mm)	64.2 GPa	0.33	49.5 MPa

$$I = 1/2\rho c\omega^2\xi^2 \qquad\qquad [1]$$

Where ρ is the density of the material, c is the velocity of ultrasonic wave propagation, ω is the angular frequency, and ξ is the ultrasonic amplitude (Tang et al., 2022). As the ultrasonic amplitude increases, the ultrasonic energy increases exponentially in a square relationship. Therefore, in the design of the simulation, the adjustment of bond power is equivalent to the control of ultrasonic frequency and ultrasonic vibration amplitude.

The parameters that affect the morphology of bonding joints are bond force, bond power and bond time. In the simulation, the force load and displacement load were regarded as

equivalent factors. Hence, the simulation scheme of bond power is realized by loading the time-varying displacement behavior of the bonding tool. The displacement load was a time-dependent function, and its mathematical expression is shown in Equation 2.

$$X = A\sin(\omega t + \varphi) \qquad [2]$$

Where A is the amplitude, ω is the angular velocity (circular frequency), f is the bonder frequency, $\omega = 2\pi f$. Stress loading $S1$ was implemented on the bond tool, which rose linearly until 30 ms and maximum to 50 N. Then, the curve of displacement load $S2$ is a sinusoidal curve with time, describing the ultrasonic action of the load on the bond tool. The sine function with a frequency of 80 kHz and an amplitude of 10 μm was set. It will be loaded on the bond tool from 0 ms. The operation time was 130 ms, with initiation parameters set in simulation models (Table 2). Substituting the parameters into the formula is $x = 10^{-5} \times \sin(1.6\pi \times 105 \times 0.13)$. A total of 9 sets of parameters were simulated (Table 3).

The bond force and ultrasonic amplitude were changed in the simulation to be the variables affecting the bonding results to explore the correlation between ultrasonic bond quality and parameters. In this project, the analysis model focused on the mechanical movement of bond tools and their stress and plastic strain and did not simulate the connection during the vibration. The vibration amplitude parameters in the FEA simulation

Table 2

Initiation parameters setting in simulation models (take an amplitude of 10 μm as an example)

Bond time (ms)	Bond force (N)	Amplitude (μm)
0	35.5 (Touch force)	10 (Vibration start)
5 (start ramp time)	36.3 (Start force)	10
25 (Bond ramp time)	50 (Bond force)	10
100 (Bond hold time)	50	10 (Vibration end)

Table 3

Bonding parameters setting in simulation models

Groups	Bond time (ms)	Bond force (N)	Amplitude (μm)
1	1× time (130)	50	10
2	1× time (130)	70	10
3	1× time (130)	100	10
4	1× time (130)	50	10
5	1× time (130)	50	20
6	1× time (130)	50	30
7	1× time (130)	50	10
8	2× time (260)	50	10
9	3× time (390)	50	10

do not match those in the real world. Hence, this research simulates other cases of higher bond force, which could show real-world situations.

The simulation results of deformation and stress can be used to evaluate the stress and mechanical behaviors of Al wire. Figure 7 shows that region (A) of the bond tool is not contacted with the wire, and region (B) of the bond tool is only contacted with the Al wire. The deformation is generated mainly in the region (D) compared to the region (C). We use letters in parenthesis, i.e., (), to define the different regions.

Refer to Figures 8a–8c for the deformation and stress simulation result. With the increase of ultrasonic amplitude and bond force, the deformation of the Al wire was intensified, and more stress was concentrated in the bottom of the Al wire. In the same group, the bond force has a more significant effect on the deformation
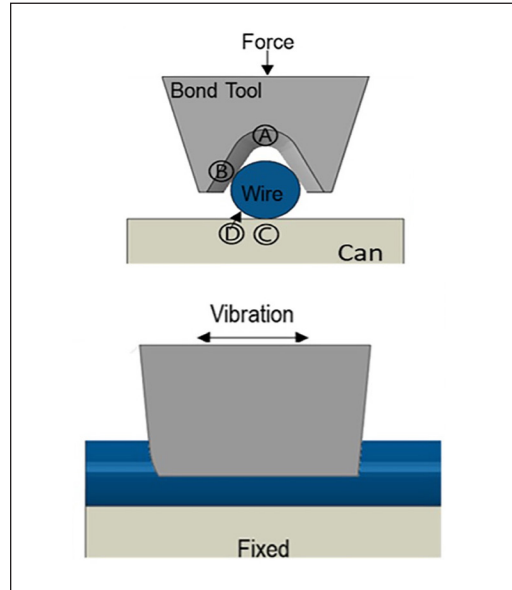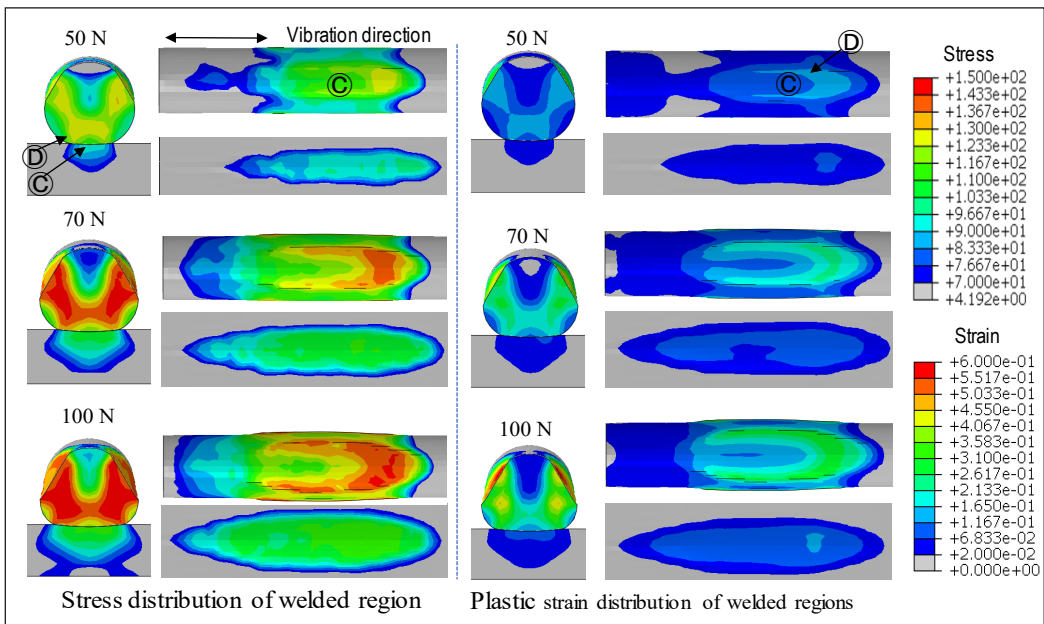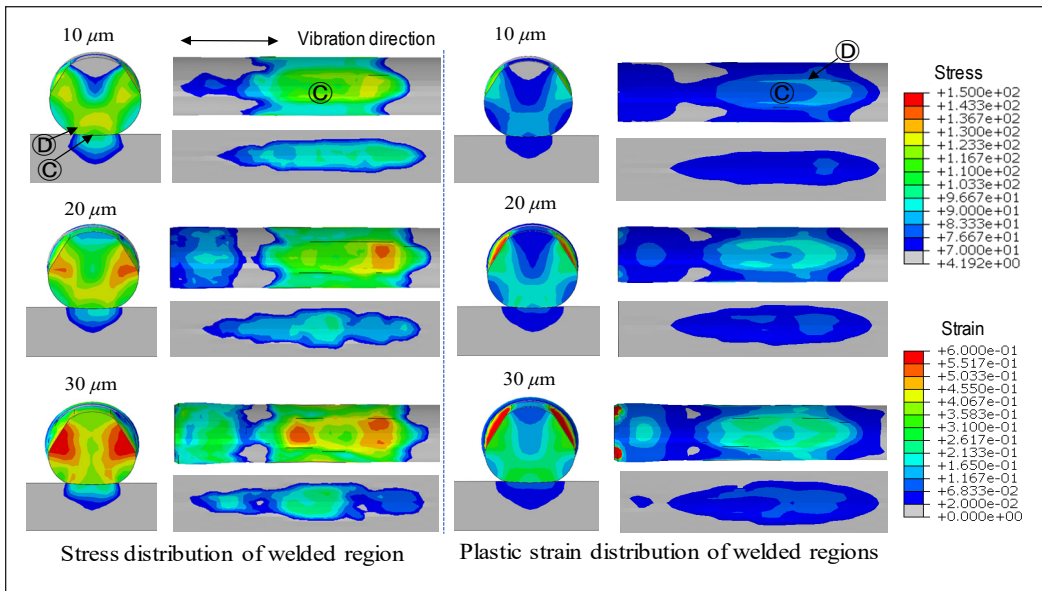

Figure 7. Schematic diagram of stress and strain distribution in different areas of the bonded component
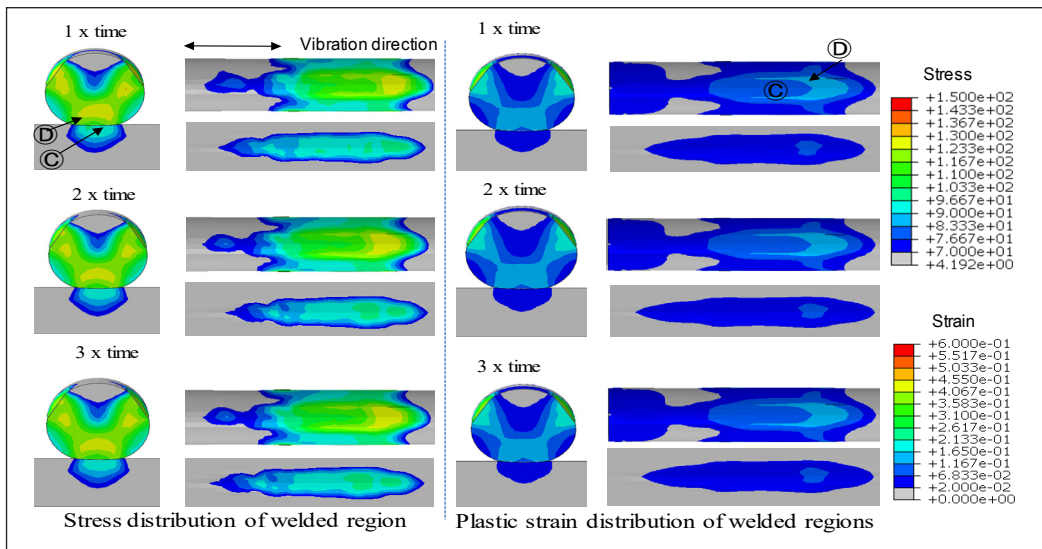

(a)

Figure 8. Simulation result under different parameters: (a) effect by bond force

(b)

(c)

Figure 8 (continue). Simulation result under different parameters: (b) effect by bond power; (c) effect by bond time

of the Al wire than the ultrasonic amplitude. Amplitude has a more significant effect on reducing the unbonded area in the center of the joint than the bond force. The maximum stress region corresponds to the bonding interface's elliptical vital ridge area. The correlation of the three parameters is as follows: First, the effect of bond force on Al wire deformation: High bond force increased the bonding area perpendicular to the wire

direction and increased stress and plastic strain levels on the bonding interface. Despite the increased bond force, region (C) remained at a lower level of stress and plastic strain compared to the surrounding area (D). Second, the effect of ultrasonic amplitudes on Al wire deformation: Due to the increased vibration amplitude of the bonding tool, the increased stress concentration occurred at the fixed end of the wire and near both endpoints. The increased amplitude condition mainly increased stress and plastic strain at the circumference region (D), compared to the stress/plastic strain at the center region (C). Third, the effect of bond time on Al wire deformation: The stress and plastic strain distributions in the bonding area do not continue to change with increasing bond time because 0.135 s is sufficient to balance the forces.

Effect of Parameter Changes on the Central Unbonded Area of the Joint

Phase I testing aims to verify the effect of bonding parameters on the unbonded area in the center of the bond interface. We performed bonding by reducing the parameter level so that we could obtain a complete bonding interface after Al wire peeling. Bond force level settings were 800 gf and 1400 gf, bond power level settings were 80 and 130, bond time settings were 100 and 160 ms, and the center point was set. A total of 27 normal cell samples with different production dates were randomly selected, and the anode surface was laser-cleaned before testing to verify the effects of bonding pressure, bonding power, and bonding time on the bonding interface morphology. There were 10 joints bonded on the anode surface of each cell and 30 joints bonded for each set of parameters, totaling 9 sets of parameters and 270 bonded joints. The results showed that the bonding interface morphology of the 30 joints was similar under the same parameter conditions. The bonding interface morphology under different parameter conditions was significantly different. A typical joint was selected for each set of parameters to observe the interface morphology under a microscope, as shown in Figure 9.

Figures 9a–9c show the interface characteristics of the bonding interface as the ultrasonic power changes. Under low bond force, only the edge of the interface is well connected, and the effective connection area is minimal. The center of the interface is not bonded. As the bonding force increases, the outline of the joint gradually expands inward. The bonding mark gradually expands toward the center, and the effective bonding area increases, but not significantly.

Figures 9d–9f show the characteristics of the bonding interface as the ultrasonic power changes. As the ultrasonic power increases, the bond mark gradually expands inward and develops from an ellipse to a circle, and the aspect ratio decreases. Under lower power, only the edge area of the interface is well connected, and the effective connection area is tiny. When the ultrasonic power increases, the unbonded area in the center area gradually decreases, and the overall effective connection area of the interface increases. Compared

with the increase in bond force, as the ultrasonic power increases, the bond mark expands more obviously to the center region, and the strong ridges' vein-shaped elliptical rings formed are more prominent.

Figures 9g–9i show the characteristics of the bonding interface as the bond time changes. Under lower power, even as the bond time increases, the bond mark gradually expands inward, which is not obvious.
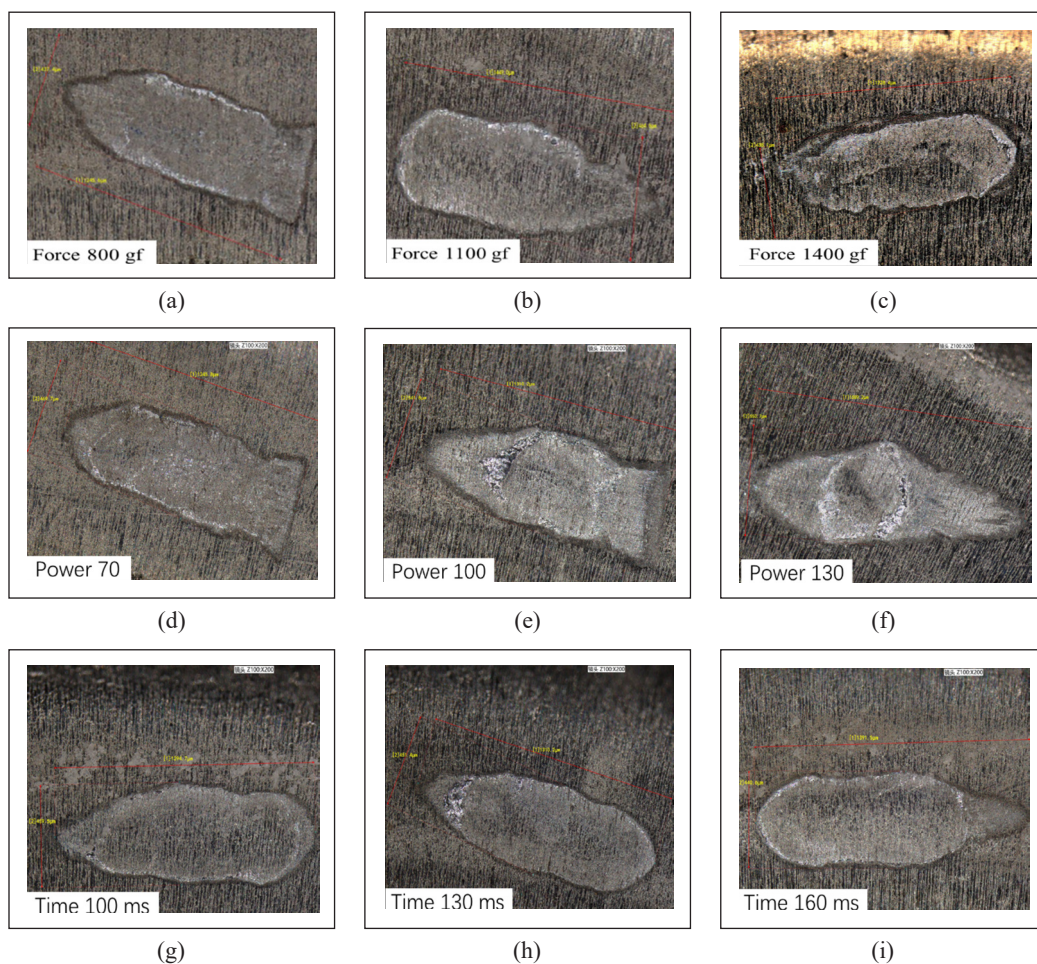
Figure 9. Effect of parameter changes on the central unbonded area of the joint: (a)–(c) Fixed: bond power: 80, bond time: 130 ms, bond force was increased; (d)–(f) Fixed: bond force 800 gf, bond time 130 ms, bond power was increased; (g)–(i) Fixed: bond force: 800 gf, bond power: 80, bond time was increased

Response Surface Methodology (RSM)

The response surface methodology (RSM) was further used in phase II. Shear strength and tensile tests were used to evaluate bonding qualities. The regression equations of aluminum wire deformation and joint width corresponding to key parameters were established.

The optimal range of Al wires deformation and joint width in lithium battery negative ultrasonic bonding is proposed. The response optimizer obtains the optimal values of bonding parameters. However, the shear strength result cannot be used as the only response to determine the parameter range because there are two failure modes in the wire bonding process. One is the contact detachment, and the corresponding minimum parameter range is obtained through shear strength. The second is neck fracture; the necking part between the joint and the Al wire is broken during the tension process, but the bonding interface maintains good connectivity. Therefore, a tensile test is required. If the bonding strength is excellent, the tensile test only shows that the Al wire breaks at the highest point of the bond loop; its fracture strength is the ultimate fracture strength of the Al wire. The data consistency is excellent. Therefore, using the tensile force as the response, the model will not fit. Hence, the maximum parameter value corresponding to the occurrence of necking fracture is obtained by testing the single variable multi-level conditions. After completing the above 2 steps, we can obtain the available parameter range through the parameter values corresponding to joint shedding and the parameter values corresponding to necking fracture.

Considering the influence of factor number and factor level number on DoE experiment number. Bond force level settings were 800 gf and 1700 gf, and bond power level settings were 80 and 130. A total of 42 normal cell samples with different production dates were randomly selected, and the anode surface was laser-cleaned before testing. There were 10 joints bonded on the anode surface of each cell and 30 joints bonded for each set of parameters, totaling 14 sets of parameters and 420 bonded joints. The standard deviation was calculated for 30 values for each set of parameters. Notice that the bond power in a bonder was dimensionless values.

The FEA simulation results confirmed that the stress and plastic strain distributions in the bonding area do not continue to change with increasing bond time because 0.135 s is sufficient to balance the bond force. So, the effect of bond time on bonding quality is no longer considered separately. The bond time is fixed at 0.135 s.

According to the analysis in Table 4, within the range of process parameters in this experiment, when the bond force was 800 gf and bond power was 80, the mean value of shear strength was 2.25 kgf. The minimum shear strength value of the abnormal point is less than 1.5 kgf (Figure 10). Therefore, it does not meet the process capability control requirement of more than 1.5 kgf. It can be concluded that when the bond force is lower than 800 gf and the bond power is lower than 80, the risk of the Al wire falling off from the bonding interface is higher. When the bond force was 1250 gf and bond power was 105, the samples' shear strength performed well, and the shear strength value was centralized. When the bond force was 1700 gf, the corresponding sample bore a large shear strength. However, the shear strength fluctuated greatly. When the bond force was 1700 gf and bond power was 130, the shear strength showed a clear downward trend.

Table 4
Experimental result of shear strength

| Std. Order	Run Order	Point Type	Blocks	Bond force (gf)	Bond power	Shear strength (Kgf)	Std. Deviation
1	2	0	2	1250	105	5.172	0.212
2	4	0	2	1250	105	4.932	0.315
3	7	0	2	1250	105	4.684	0.285
4	8	1	1	1700	80	4.157	0.261
5	9	1	1	800	80	2.250	0.229
6	10	0	1	1250	105	4.983	0.293
7	11	1	1	800	130	4.182	0.274
8	12	0	1	1250	105	4.681	0.256
9	13	1	1	1700	130	3.818	0.443
10	14	0	1	1250	105	4.602	0.277
11	1	-1	2	800	105	4.078	0.163
12	3	-1	2	1250	80	3.173	0.161
13	5	-1	2	1250	130	4.575	0.324
14	6	-1	2	1700	105	4.915	0.253
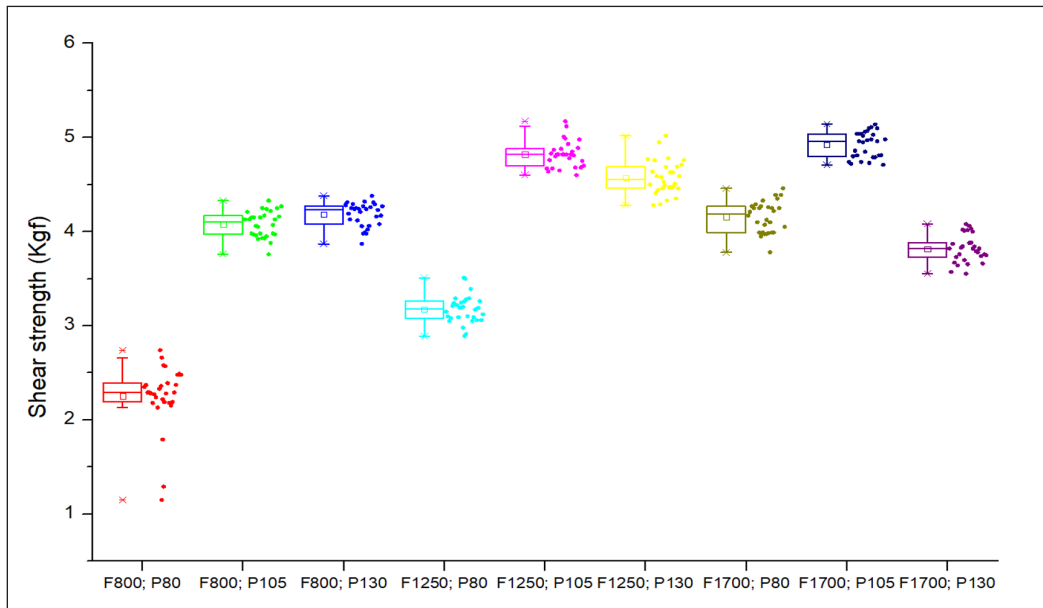
Figure 10. Box plot of shear strength under different parameters

Table 5 and Figure 11 show that bond power had a more significant impact on the width of bonding joint forming than bond force. Table 6 shows that bond force had a more substantial effect on the deformation amount (i.e., Z-axis displacement of the bond tool) of bonding joint forming than bond power. From the standard deviation distribution, the more
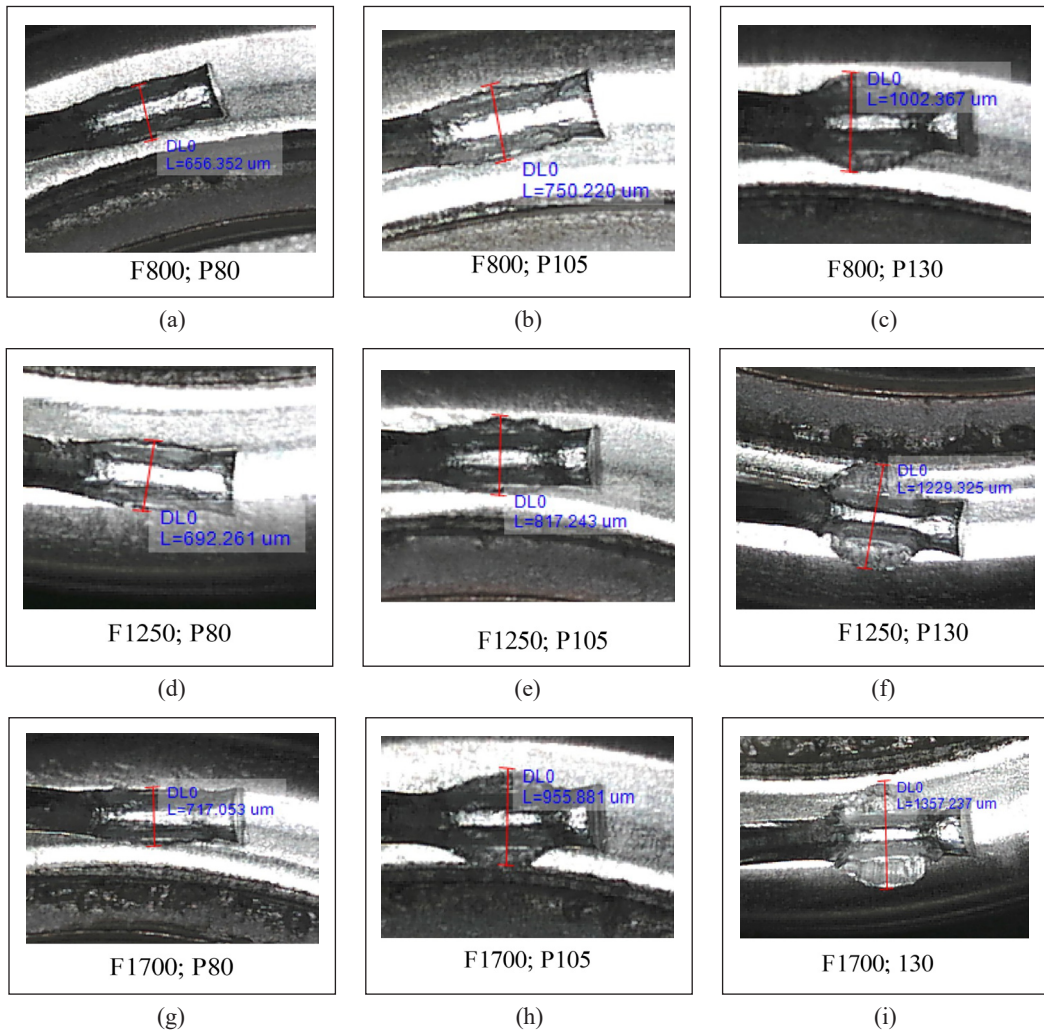
Figure 11. Joint width profile under different parameters: (a)–(c) Fixed: bond force: 800, bond power was increased; (d)–(f) Fixed: bond force 1250 gf, bond power was increased; (g)–(i) Fixed: bond force: 1700 gf, bond power was increased

significant standard deviation means that it was more challenging to control the stability and bonding accuracy of the results.

The failed samples with shear strength lower than 1.5 kgf were analyzed separately, and it was found that the reasons for failure were different. Can surface contamination caused by residual F components in the electrolyte is one of the main reasons? The x-ray photoelectron spectroscopy (XPS) analysis result showed that NiO, NiF_2, and Ni $(OH)_2$ are confirmed on the can surface. The flatness exceeds the specification of the canned surface (R angle size), which are other factors that influence it. The failure caused by these noise factors should not be confused with the failure caused by unreasonable parameters.

Table 5
Experimental result of joint width

Std. Order	Run Order	Point Type	Blocks	Bond force (gf)	Bond power	Joint width (μm)	Std. Deviation
1	2	0	2	1250	105	809.426	20.14
2	4	0	2	1250	105	824.742	22.11
3	7	0	2	1250	105	797.215	22.31
4	8	1	1	1700	80	727.895	18.34
5	9	1	1	800	80	659.812	15.44
6	10	0	1	1250	105	806.380	21.63
7	11	1	1	800	130	1102.264	29.94
8	12	0	1	1250	105	805.674	20.15
9	13	1	1	1700	130	1445.003	29.26
10	14	0	1	1250	105	793.673	20.13
11	1	-1	2	800	105	778.068	29.048
12	3	-1	2	1250	80	682.397	18.17
13	5	-1	2	1250	130	1273.353	22.46
14	6	-1	2	1700	105	945.726	19.44

Table 6
Experimental result of deformation amount

Std. Order	Run Order	Point Type	Blocks	Bond force (gf)	Bond power	Deformation amount (μm)	Std. Deviation
1	2	0	2	1250	105	206.645	11.18
2	4	0	2	1250	105	202.250	11.25
3	7	0	2	1250	105	208.272	11.95
4	8	1	1	1700	80	216.600	12.04
5	9	1	1	800	80	162.500	10.60
6	10	0	1	1250	105	199.520	10.63
7	11	1	1	800	130	202.500	12.51
8	12	0	1	1250	105	200.400	11.56
9	13	1	1	1700	130	262.700	13.26
10	14	0	1	1250	105	202.520	9.26
11	1	-1	2	800	105	179.485	9.05
12	3	-1	2	1250	80	187.340	12.17
13	5	-1	2	1250	130	227.500	11.65
14	6	-1	2	1700	105	238.500	12.44

Tensile Testing

In this phase, the purpose of the tensile test is to exclude abnormal joints of bonding strength less than Al wire fracture strength; it can also exclude abnormal joints of neck fracture and then obtain the minimum parameter range of the bonded joint neck fracture. In the tensile

test, two main failure modes were neck fracture and Al wire overall or party fall off. The overall and partial detachment of joints indicates that the bonding interface is weakly bonded, and the joints with neck fractures suggest that the aluminum wire at the root of the joint is abnormally deformed. Still, the bonding strength of the bonding interface is good.

The automatic pulling force and over-travel distance must be set to reasonable parameters to enable inspection without damaging the Al wire. Automatic pulling inspection is applied to a single bonding point and only detects bonding points with bonding strength less than 0.60 kgf.

A manual tensile test is suitable for sampling checks. It is on a complete bonding loop, and the pulling force is used at the highest point of the Al wire bond loop. The maximum breaking strength of the Al wire loop at the highest point between two bonding points is about 76 N/mm^2, which is approximately equal to 1.52 kgf (i.e., 0.1963 mm^2 × 76 N/mm^2 = 14.9 N = 1.52 kgf). For this reason, to ensure that the bonding strength is greater than the breaking strength of the Al wire, the tensile strength requirement for bonded joints is greater than 1.5 kgf when performing a tensile test on a complete bond loop.

The tensile test result is shown in Table 7. High bond force and high bond power significantly influenced the neck fracture. The neck fracture occurred when the bond force was 1600 gf and the bond power was 130. However, the bonded joint fall-off occurred at bonder force was 900 gf and bond power less than 90. The fractures occurred at the highest point of the bond loop for the sample group without neck fracture. Due to the consistency of the Al wire in the experiment, the data fluctuates slightly. For the sample group with good bonding strength, the tensile force at the highest point of the bond loop ranges from 1212 gf to 1520 gf. This is consistent with the breaking strength limit of the Al wire in Figure 6.

Table 7
Experimental result of tensile test (unit: gf)

Force	Power						
	80	90	100	110	120	125	130
800	Fall off <1.5 kgf	Fall off <1.5 kgf	1489	1391	1406	1511	1360
900	Fall off <1.5 kgf	1214	1299	1313	1303	1216	1215
1000	1365	1329	1414	1516	1520	1312	1424
1100	1264	1505	1326	1412	1328	1254	1261
1200	1412	1413	1382	1501	1411	1324	1311
1300	1386	1274	1471	1428	1375	1263	1287
1400	1352	1342	1335	1314	1520	1314	1345
1500	1326	1426	1420	1323	1431	1321	1376
1600	1245	1283	1338	1314	1302	1151	Neck fracture
1700	1212	1312	1325	1227	1158	Neck fracture	Neck fracture

Typical Joint Analysis

The morphological characteristics of the joint show that the shape of the bonding joint is elliptical. Bonding starts from the periphery of the ellipse and gradually spreads to the central area. The effective bonding area is the ridges' vein-shaped elliptical rings, and the central area is not bonded. The aspect ratio of the unbonded area of each sample also varies significantly.

Furthermore, under the difference parameter condition, the interface characteristics of the joint vary significantly. Under low bond force, only the edge of the interface is well connected, and the effective connection area is minimal. As the bonding force increases, the outline of the joint gradually expands inward. The bonding mark gradually expands toward the center, and the effective bonding area increases, but not significantly. As the ultrasonic power increases, the bond mark gradually expands inward and develops from an ellipse to a circle, and the aspect ratio decreases. Under lower power, only the edge area of the interface is well connected, and the effective connection area is tiny. When the ultrasonic power increases, the unbonded area in the center area gradually decreases, and the overall effective connection area of the interface increases. Compared with the increase in bond force, as the ultrasonic power increases, the bond mark expands more obviously to the center region, and the strong ridges' vein-shaped elliptical rings formed are more prominent. In contrast, under lower power and low bond force, even as the bond time increases, the bond mark expansion inward is not obvious.

## Simulation Prediction and Process Test Verification

The stress and plastic strain simulation results show that the increase in bond force and amplitude generated a large deformation and increased stress/plastic strain level. Despite the rise in the bond force and amplitude, the stress/plastic strain at the center region (C) is lower than that in the circumference region (D). The stress and plastic strain distributions in the bonding area do not continue to change with increasing bonding time because 0.135 s is sufficient to balance the forces. The maximum stress region corresponds to the bonding interface's elliptical vital ridge area. The stress distribution feature offers some explanations of the central region pattern. Due to the increased vibration amplitude of the bonding tool, the increased stress concentration occurred at the fixed end of the Al wire and near both endpoints. The increase in the amplitude has a more significant effect on the diffusion of the elliptical vital ridge toward the central area.

Based on the DoE implemented in phase I, the unbonded area in the center region of joints can be limitedly reduced by optimizing significant parameters. The influencing parameters in the most to least critical order are bond power, bond force, and bond time. Based on the RSM analysis result in phase II, bond power had a more significant impact on the width of joint forming than bond force. The bond force had a more substantial effect on the deformation amount (i.e., Z-axis displacement of the bond tool) of bonding

joint forming than bond power. According to the failure mode in tensile test results, the range of bond force is at least greater than or equal to 900 gf and cannot exceed 1700 gf. The bond power is at least greater than or equal to 90 and cannot exceed 120. The optimal shear strength distribution is in the range of 3.5 kgf to 4.75 kgf after combining the optimal parameter range obtained from the shear strength and tensile tests and the results of the contour plot (Figure 12a). Therefore, the response optimizer sets the shear strength target value to 4.75 kgf. So far, the optimal parameter values are bond force 1250 gf and bond power 100, as shown in Figure 12b. The bonding joint and process parameters regression equation was derived from the deformation data, as shown in Equation 3.
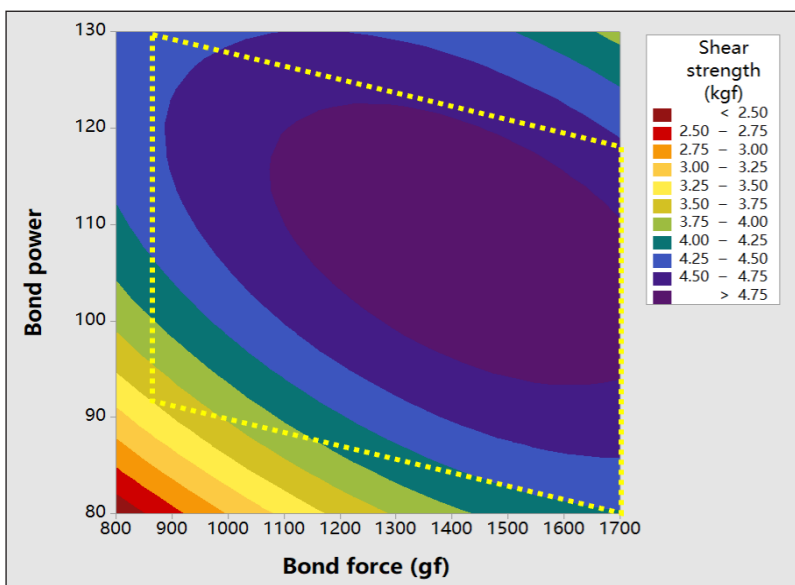
(a)
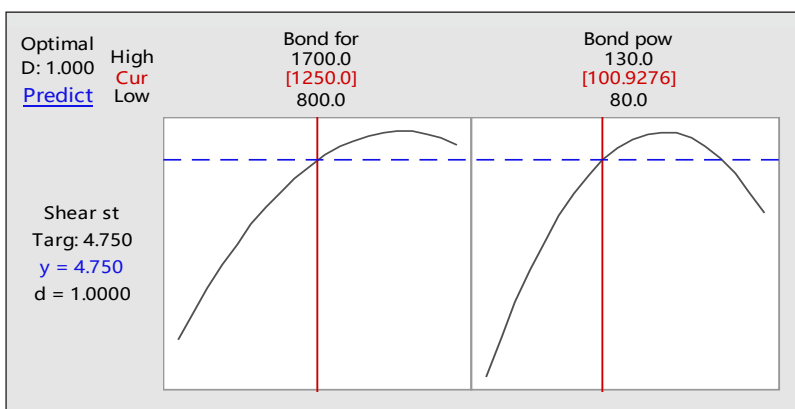
(b)

Figure 12. (a) Contour plot of shear strength vs bond power, bond force; (b) The optimal parameters obtained by the response optimizer

$$D_e = 118.3 + 0.0154F_e - 0.063P_e + 0.000022\ F_e{}^2 + 0.0045\ P_e{}^2 - 0.000087\ F_eP_e \qquad [3]$$

D_e represents the deformation of the bonding joint, F_e represents the actual bond force, and Pe represents the bond power of the bonding machine. The minimum value in this region was 174 μm, and the maximum value was 248 μm. The bonding joint and process parameters regression equation was derived from the joint width data, as shown in Equation 4.

$$W_e = 3005 - 0.802\ F_e - 48.51\ P_e + 0.000153\ F_e{}^2 + 0.2502\ P_e{}^{2+} + 0.006103\ F_eP_e \qquad [4]$$

W_e represent the width of the bonding joint. The minimum value of the width was 560 μm, and the maximum value of the width was 1110 μm.

In the actual application, the bonding parameters are set to the optimal values of the bond force of 1250 gf and bond power of 100, dramatically reducing the unbonded area in the center region of joints. The morphology of the bonding interface is shown in Figure 13.

The DoE results proved that bond power and force positively affected the bonding joint's reliability in a specific range. However, they will cause an opposite result outside the range, such as a neck fracture or unbonded.
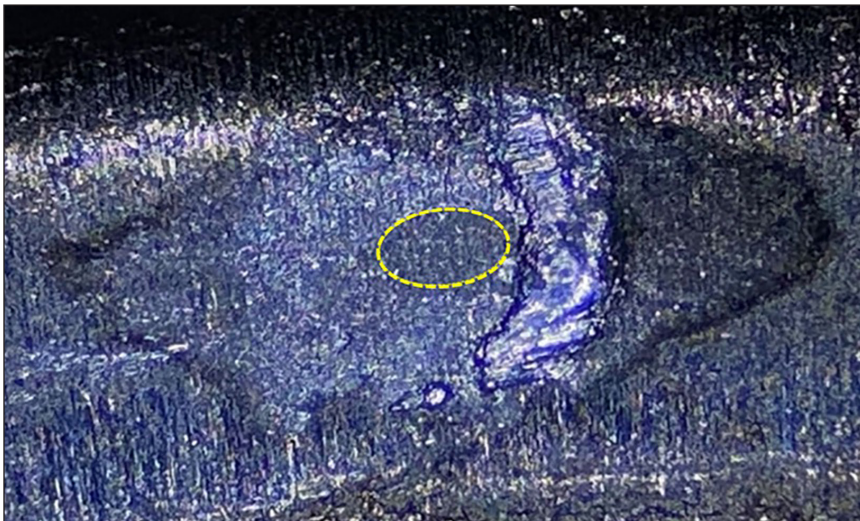

Figure 13. The morphology of the bonding interface under optimal parameter (F: 1250 gf; P: 100)

CONCLUSION

This paper demonstrates that combined experimental and simulation methods can determine the most important wire bonding parameter of the negative terminal (Al wire and Fe-base Ni-top can shell) in 21700 cylindrical lithium battery modules. The effect of parameter changes on the central unbonded area of the joint is analyzed using intermetallic layer and visual analysis. The reasons for the poor bonding performance of the central area of the

joint through stress and strain simulation. The results show that the interface mode of Al-Ni ultrasonic wedge bonding is shaped like a ridged torus, and the center area is unbounded. Ridge wrinkles are high-strength bonding formed by strong physical diffusion under the action of ultrasound. These ridge wrinkles form the bonding strength. Second, the stress at the center region (C) is lower than that in the circumference region (D), and the high-stress region corresponds to the elliptical shape strong ridge area of the bonding interface (i.e., the effective bonding area). Third, optimizing parameters can limit the unbonded area in the center region of joints, and the influencing parameters in the order of most to least significant are bond power, bond force, and bond time. iv. the best shear strength range is 3.5 kgf to 4.75 kgf, and the optimal range of the Al wire deformation amount was 174 μm to 248 μm. The optimal range of joint width was 560 μm to 1110 μm. v. the best parameter range is bond force 900 gf to 1700 gf and bond power 90 to 120. Within this range, no joint fall-off and necking fracture will occur. The simulation and DoE results above provided a new feasible scheme for rapidly finding the optimal process parameters in the bonding process.

ACKNOWLEDGMENT

REFERENCES

Bieliszczuk, K., Chmielewski, T. M., & Zręda, J. (2024a). Selected properties of aluminum ultrasonic wire bonded joints with nickel-plated steel substrate for 18650 cylindrical cells. *Journal of Advanced Joining Processes*, *9*, Article 100197 https://doi.org /10.1016/j.jajp.2024.100197

Bieliszczuk, K., Chmielewski, T. M., & Zręda, J. (2024b). Influence of cylindrical cells surface cleaning by means of laser ablation on wedge wire bonding process. *Coatings, 14*(4), Article 445.

Chang, H. S., Hsieh, K. C., Martens, T., & Yang, A. (2004). Wire bond void formation during high-temperature aging. *IEEE Transactions on Components and Packaging Technologies, 27*(1), 155–160. https://doi.org/10.1109/TCAPT.2004.825752

Chen, X., Zhong, Z., & Li, J. (2006). Analysis on characteristics of input power and interface wedge bonding of Al-Ni ultrasonic aluminum wedge bonds. *Material Science and Technology, 14*(4), 416–419.

Czerny, B., & Khatibi, G. (2016). Interface reliability and lifetime prediction of heavy aluminum wire bonds. *Microelectronics Reliability, 58*, 65–72. https://doi.org /10.1016/j.microrel.2015.11.028

Czerny, B., Khatibi, G., Paul, I., & Thoben, M. (2013). Influence of wirebond shape on its lifetime with application to frame connections. In *2013 14th International Conference on Thermal, Mechanical and Multi-Physics Simulation and Experiments in Microelectronics and Microsystems (EuroSimE)* (pp. 1-5). IEEE Publishing. https://doi.org/10.1109/EuroSimE.2013.6529909

Hamada, K., & Iwamoto, C. (2023). Morphology and microstructure observation of cemented carbide tool with surface wear and Al adhesion for Al wedge wire bonding. *Journal of Light Metal Welding, 61*(10), 492–499. https://doi.org/10.11283/jlwa.61.492

Harman, G. G., & Albers, J. (1977). The ultrasonic welding mechanism as applied to aluminum and gold-wire bonding in microelectronics. *IEEE Transactions on Parts, Hybrids, and Packaging, 13*(4), 406–412. https://doi.org/10.1109/TPHP.1977.1135225

Ho, J., Chen, C., & Wang, C. (2004). Thin film thermal sensor for real time measurement of contact temperature during ultrasonic wire bonding process. *Sensors & Actuators: A. Physical, 111*(2), 188–195. https://doi.org/10.1016/j.sna.2003.10.018

Ji, H., Li, M., & Wang, C. (2006). Interfacial characterization and bonding mechanism of ultrasonic wedge bonding. In *2006 7th International Conference on Electronic Packaging Technology* (pp. 1-5). IEEE Publishing. https://doi.org/10.1109/ICEPT.2006.359760

Ji, H., Li, M., Kung, A. T., Wang, C., & Li, D. (2005). The diffusion of Ni into Al wire at the interface of ultrasonic wire bond during high-temperature storage. In *2005 6th International Conference on Electronic Packaging Technology* (pp. 377-381). IEEE Publishing. https://doi.org/10.1109/ICEPT.2005.1564652

Li, J., Han, L., Duan, J., & Zhong, J. (2007a). Microstructural characteristics of Au/Al bonded interfaces. *Material Characterization,58*(2), 103-107. https://doi.org/10.1016/j.matchemphys.2007.06.034

Li, J., Han, L., Duan, J., & Zhong, J. (2007b). Interface mechanism of ultrasonic flip chip bonding. *Applied Physics Letters, 90*(24), Article 242902. https://doi.org/10.1063/1.2747673

Li, J., Han, L., Duan, J., & Zhong, J. (2007c). Microstructural characteristics of Au/Al bonded interfaces. *Materials Characterization, 58*(2), 103–107. https://doi.org/10.1016/j.matchar.2006.03.018

Li, L., Xu, S., Liang, Y. K., & Wei, P. (2019). 10 mils Al wire heavy wedge bond wire deformation thickness study. In *2019 20th International Conference on Electronic Packaging Technology (ICEPT)* (pp. 1-4). IEEE Publishing. https://doi.org/10.1109/ICEPT47577.2019.245791

Li, M., Ji, H., Wang, C., Bang, H. S., & Bang, H. S. (2006). Interdiffusion of Al–Ni system enhanced by ultrasonic vibration at ambient temperature. *Ultrasonics, 45*(1–4), 61–65. https://doi.org /10.1016/j.ultras.2006.06.058.

Long, Y., Li, C., Twiefel, J., Wallaschek, J., Schneider, F., & Hermsdorf, J. (2019). Quantification of the energy flows during ultrasonic wire bonding under different process parameters. *International Journal of Precision Engineering and Manufacturing-Green Technology, 6*(3), 449–463. https://doi.org/10.1007/s40684-019-00061-0

Long, Y., Twiefel, J., & Wallaschek, J. (2020). Contact mechanics and friction processes in ultrasonic wire bonding - Basic theories and experimental investigations. *Journal of Sound and Vibration, 468,* Article 115021. https://doi.org/10.1016/j.jsv.2019.115021

Lum, I., Jung, J. P., & Y. Zhou. (2005). Bonding mechanism in ultrasonic gold ball bonds on copper substrate. *Metallurgical & Materials Transactions. Part A, 36*(5), 1279–1286. https://doi.org /10.1007/s11661-005-0220-2

Lum, I., Mayer, M., & Zhou, Y. (2006). Footprint study of ultrasonic wedge-bonding with aluminum wire on copper substrate. *Journal of Electronic Materials, 35*(3), 433–442. https://doi.org /10.1007/BF02690530

Mindlin, R. D. (1949). Compliance of elastic bodies in contact. *Journal of Applied Mechanics, 16*(3), 259–268. https://doi.org/10.1115/1.4009973

Qi, J., Hung, N. C., Li, M., & Liu, D. (2006). Effects of process parameters on bondability in ultrasonic ball bonding. *Scripta Materialia*, *54*(2), 293–297. https://doi.org/10.1016/j.scriptamat.2005.07.042

Schemmel, R., Althoff, S., Sextro, W., Unger, A., Hunstig, M., & Brökelmann, M. (2018a). Effects of different working frequencies on the joint formation in copper wire bonding. In *CIPS 2018; 10th International Conference on Integrated Power Electronics Systems* (pp. 1-6). VDE Publishing.

Schemmel, R., Hemsel, T., & Sextro, W. (2018b, June 11-15). *Numerical and experimental investigations in ultrasonic heavy wire bonding.* [Paper presentation]. Proceedings of the 6th European Conference on Computational Mechanics: Solids, Structures and Coupled Problems, ECCM 2018 and 7th European Conference on Computational Fluid Dynamics, Glasgow, United Kingdom.

Tang, J., Li, L., Zhang, G., Zhang, J., & Liu, P. (2022). Finite element modeling and analysis of ultrasonic bonding process of thick aluminum wires for power electronic packaging. *Microelectronics Reliability, 139*, Article 114859. https://doi.org /10.1016/j.microrel.2022.114859

Unger, A., Schemmel, R., Meyer, T., Eacock, F., Eichwald, P., Althoff, S., Sextro, W., Brokelmann, M., Hunstig, M., & Guth, K. (2016). Validated simulation of the ultrasonic wire bonding process. In *2016 IEEE CPMT Symposium Japan (ICSJ)* (pp. 251-254). IEEE Publishing. https://doi.org/10.1109/ICSJ.2016.7801275

Uno, T., & Tatsumi, K. (2000). Thermal reliability of gold–aluminum bonds encapsulated in bi-phenyl epoxy resin. Microelectronics Reliability, 40(1), 145–153. https://doi.org/10.1016/S0026-2714(99)00087-6

Winchell, V. H., & Berg, H. M. (1978). Enhancing ultrasonic bond development. *IEEE Transactions on Components, Hybrids, and Manufacturing Technology, 1*(3), 211–219. https://doi.org /10.1109/ TCHMT.1978.1135291

Zhou, Y., Li, X., & Noolu, N. J. (2005). A footprint study of bond initiation in gold wire crescent bonding. *IEEE Transactions on Components & Packaging Technologies, 28*(4), 810–816. https://doi.org /10.1109/ TCAPT.2005.848585

Zwicker, M. F. R., Moghadam, M., Zhang, W., & Nielsen, C. V. (2020). Automotive battery pack manufacturing – A review of battery to tab joining. *Journal of Advanced Joining Processes, 1,* Article 100017. https:// doi.org/10.1016/j.jajp.2020.100017